

中国激光

激光粉末床熔化制备 TiB₂颗粒增强 7050 铝基复合材料的组织及性能研究(特邀)

王安¹, 唐梓珏^{1,2}, 吴一^{1,2}, 王浩伟^{1,2}, 王洪泽^{1,2*}

¹ 上海交通大学材料科学与工程学院金属基复合材料国家重点实验室, 上海 200240;

² 上海交通大学安徽(淮北)陶铝新材料研究院, 安徽 淮北 235000

摘要 采用激光粉末床熔化(LPBF)工艺制备 TiB₂质量分数为 7% 的原位自生 7050 铝基复合材料, 研究了沉积态及热处理(在 475 °C 的条件下固溶处理 1 h 后, 再在 120 °C 的条件下时效处理 12 h)后 TiB₂/7050 复合材料的微观组织和室温拉伸性能的变化。结果表明: 纳米量级尺寸 TiB₂颗粒的加入能显著抑制 LPBF 成形 7050 铝合金裂纹的产生, 且采用 LPBF 工艺制备的 TiB₂/7050 复合材料表现出较好的成形性。在激光功率为 240 W、扫描速度为 450 mm/s 及扫描间距为 75 μm 的工艺参数组合下, 沉积态 TiB₂/7050 复合材料的最大抗拉强度、屈服强度和延伸率分别为 (282±4) MPa、(246±4) MPa 和 (2.5±0.2)%; 热处理后, TiB₂/7050 复合材料的抗拉强度、屈服强度和延伸率分别达到 (346±5) MPa、(289±5) MPa 和 (4±0.2)%。此结果接近现有文献报道的第二相颗粒增强 7050 铝合金的力学性能, 并进一步降低了粉末制备成本。采用 LPBF 工艺制备的 TiB₂/7050 复合材料的主要强化机制是析出相强化、位错强化、晶界强化及 TiB₂和第二相颗粒带来的 Orowan 强化, 热处理后获得较好的综合室温拉伸性能。

关键词 激光技术; 激光粉末床熔化; TiB₂/7050 复合材料; 热处理; 力学性能

中图分类号 TG146.2 文献标志码 A

DOI: 10.3788/CJL231210

1 引言

激光粉末床熔化(LPBF)属于金属增材制造技术, 利用高功率激光熔化粉末材料^[1-3], 通过逐层堆叠打印, 可以制造形状复杂且集结构与功能于一体的构件, 与传统铸造技术相比, 具有独特的优点^[4-6]。然而, LPBF 工艺能加工的金属材料种类非常有限。目前 LPBF 成形的铝合金主要集中在 Al-Si 系, 而关于其他铝合金的研究报道相对较少^[7-8]。所以研究其他传统铝合金材料的打印性能以及设计新的铝合金材料成分很有必要^[9]。

7xxx 系铝合金具有极强的力学性能及耐磨性能, 被广泛应用在汽车等领域中^[10]。而 7050 铝合金是具有代表性的 7xxx 系铝合金之一, 它具有较高的抗拉强度及较强的抗应力腐蚀性能, 被应用在飞机舱壁等长期服役的环境中^[11]。相较于传统的铸造、轧制等制备方法, 使用 LPBF 技术制备 7050 铝合金复杂零部件具有更大的优势。然而, 7050 铝合金具有本征不可焊性, 而增材制造过程中的快速冷却会产生高热应力, 故其在 LPBF 制备过程中会发生开裂或变形, 这限制了 LPBF 技术在该合金制备中的应用^[12-13]。目前关于

7xxx 系铝合金的研究工作主要集中在 7075 铝合金方面^[14-18], 同时也有少量关于 7050 铝合金的研究^[19-20]。2017 年, Martin 等^[17]使用静电组装技术制备出均匀分布的颗粒增强 7075 高强铝合金粉体。在这种粉体中, ZrH₂ 纳米颗粒作为异质形核质点均匀地分布在 7075 高强铝合金粉体的表面上, 起到了细化晶粒的作用。由于柱状晶转变为各方向上尺寸相差较小的等轴晶, 7075 高强铝合金的热裂敏感性降低, 抗热裂性能增强, 从而实现了 LPBF 成形无裂纹的目标。此外, 詹强坤等^[21]使用低能球磨法制备了 ZrH₂/7075 复合粉末, 并研究了 ZrH₂ 纳米颗粒对试样的显微组织和力学性能的影响。同样, Mertens 等^[19]在 7050 铝合金中添加了质量分数为 1% 的 Zr, 经过固溶处理和时效处理后, 该材料的抗拉强度超过 400 MPa。Zr 元素的添加可以细化铝合金的晶粒并且降低材料的热裂倾向, 从而提高 LPBF 的成形质量, 达到增强原有合金力学性能的目的。但是, 此方法产生的细化晶粒有限, 且初生的 Al₃Zr 相在激光成形过程中会发生熔解, 无法起到形核质点的作用^[22]。此外, Li 等^[20]将 Ti/TiN 混合晶粒细化剂添加到 LPBF 成形的 7050 铝合金中, 获得了平均尺寸为 775 nm 的超细晶粒。相较于 7075 铝合金,

收稿日期: 2023-09-15; 修回日期: 2023-10-18; 录用日期: 2023-11-30; 网络首发日期: 2023-12-12

基金项目: 国家自然科学基金(52075327, 52004160, 52105469)、中国博士后科学基金(2021M692038)

通信作者: *hz.wang@sjtu.edu.cn

7050 铝合金中的 Zn 和 Cu 含量发生变化, 而这两种元素含量的变化都会使 7050 铝合金的熔点发生改变, 最终影响 LPBF 过程中该合金的裂纹量, 增加了打印难度。因此, 需要采用适当的激光工艺参数, 确保 7050 铝合金能够完全熔化, 并尽可能减少热影响区域中产生的裂纹和变形。

本文采用 LPBF 成形 TiB₂/7050 复合材料, 后续采用热处理(固溶处理+时效处理)工艺处理材料, 研究了不同工艺参数及热处理状态对 TiB₂/7050 复合材料的微观组织和室温拉伸性能的影响, 并得到了无裂纹且力学性能良好的 LPBF 成形 TiB₂/7050 复合材料。

2 材料与实验设备

采用原位自生混合盐法制备含有 7% (质量分数) TiB₂ 的 7050 铝合金铸锭。采用气雾化制粉工艺, 得到粒径为 15~53 μm 的 TiB₂/7050 复合材料粉末^[23]。电感耦合等离子体(ICP)检测结果如表 1 所示。图 1(a)

为 TiB₂/7050 复合材料粉末的表面形貌, 可以发现 TiB₂/7050 复合材料粉末具有较高的球形度, 适合作为 LPBF 的原材料。采用 3D 打印机进行成形, 基板选用轧制态 7050 铝合金, 对其进行砂纸打磨和无水乙醇清洗, 以确保基板表面洁净平整。在成形过程中, 腔体内 O₂ 的体积分数不超过 0.02%。采用正交方法选择激光工艺参数, 其中激光功率分别为 210、225、240、255 W, 扫描速度分别为 400、450、500、550、600 mm/s, 扫描间距分别为 75 μm 和 90 μm。在旋转 90° 的层间扫描策略下 LPBF 成形试样的实物图如图 1(b)所示, 共 40 组, 试样尺寸为 10 mm × 10 mm × 10 mm。对打印的成形试样进行机械研磨和抛光, 采用光学显微镜(OM)观察试样的截面金相组织, 选取其中孔隙相对较少的试样进行后续拉伸试样的制作。LPBF 成形的尺寸为 60 mm × 20 mm × 10 mm 的样块如图 1(c)所示, 之后利用线切割工艺制作长度为 54.5 mm 的标准拉伸片, 研磨抛光处理后拉伸试样的形状及尺寸如图 1(d)所示。

表 1 TiB₂/7050 复合材料粉末及 LPBF 成形试样的化学成分
Table 1 Chemical compositions of TiB₂/7050 composite powder and LPBF formed sample

Material	Mass fraction /%						
	Zn	Mg	Cu	Zr	Ti	B	Al
TiB ₂ /7050 composite powder	6.641	2.345	2.121	0.135	4.963	2.149	Bal.
LPBF formed sample	4.593	1.755	2.288	0.143	4.895	2.133	Bal.

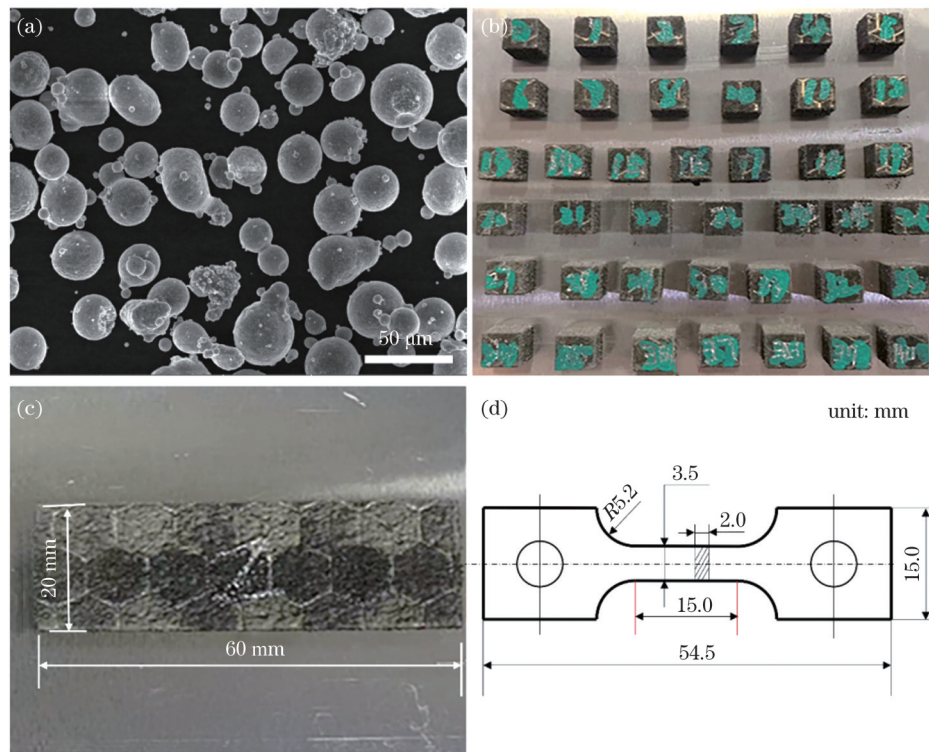


图 1 TiB₂/7050 复合材料粉末形貌、打印试样块及拉伸试样尺寸。(a)粉末形貌;(b)不同的打印样块;(c)LPBF 成形的尺寸为 60 mm × 20 mm × 10 mm 的样块;(d)拉伸试样尺寸示意图

Fig. 1 TiB₂/7050 composite powder morphology, print sample blocks, and tensile sample size. (a) Powder morphology; (b) different print sample blocks; (c) LPBF shaped sample block with size of 60 mm × 20 mm × 10 mm; (d) schematic of tensile specimen size

本文采用的热处理为单级固溶处理+时效处理,首先将样品在 475 °C 固熔炉中放置 1 h,然后放到室温水中进行冷却,再在 120 °C 的时效炉中放置 12 h,最终在空气中冷却。室温拉伸实验在拉伸设备中进行,其中应变速率采用 10^{-4} s^{-1} 。对三个同等状态的拉伸试样进行测试,结果取平均值。采用 X 射线衍射仪分析样品的物相组成,衍射角度在 20°~120° 范围内,扫描速率为 2 (°)/min。微观组织表征采用扫描电子显微镜(SEM),并利用能谱仪(EDS)分析材料表面的元素组成。采用三离子束切割仪,通过机械研磨和离子抛光,制备电子背散射衍射(EBSD)样品。使用配有 EBSD 检测器的 SEM 对样品进行显微结构分析,其中 EBSD 分析采用 1.8 μm 的步长,EBSD 菊池花样使用 Aztec 晶体软件包进行处理。

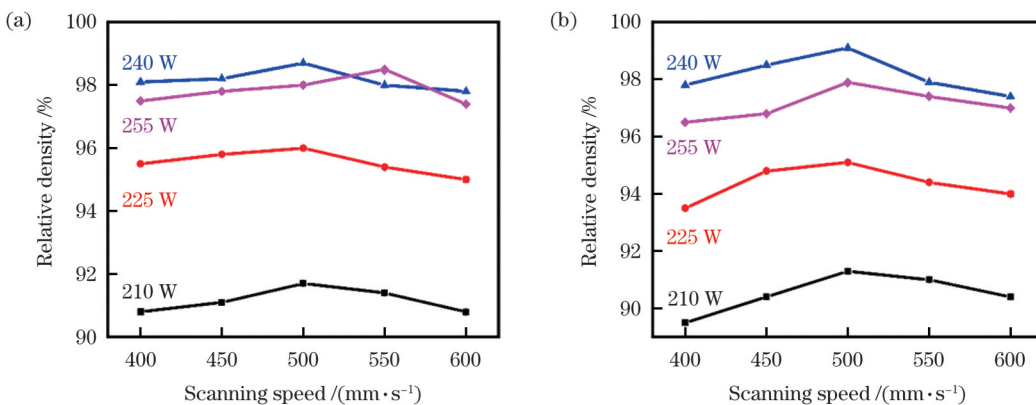


图 2 不同扫描间距下样块的相对密度。(a)扫描间距为 75 μm ; (b)扫描间距为 90 μm

Fig. 2 Relative density values of samples measured under different scanning spacings. (a) Scanning spacing of 75 μm ; (b) scanning spacing of 90 μm

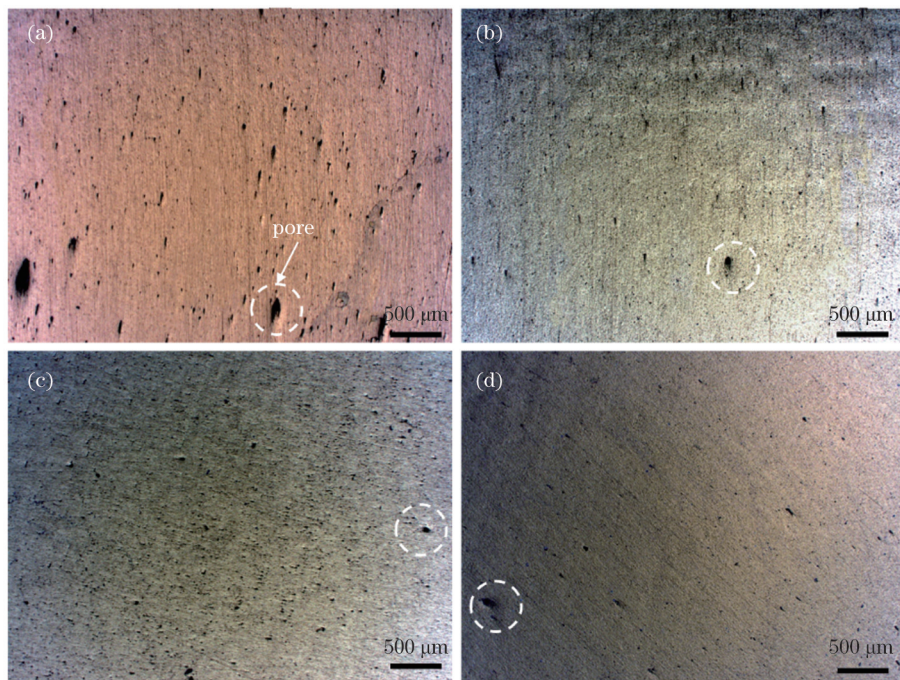


图 3 不同工艺参数下的 $\text{TiB}_2/7050$ 截面金相组织。(a)No.1;(b)No.2;(c)No.3;(d)No.4

Fig. 3 Metallographic structures of $\text{TiB}_2/7050$ sections under different process parameters. (a) No.1; (b) No.2; (c) No.3; (d) No.4

3 分析与讨论

3.1 试样块的微观组织

采用阿基米德排水法测量 40 组不同打印参数下的 $\text{TiB}_2/7050$ 复合材料试样的相对密度,结果如图 2 所示。其中,在以下四组工艺参数(激光功率 + 扫描速度 + 扫描间距)下,打印试样的相对密度较高:240 W+450 mm/s+75 μm (No.1), 240 W+500 mm/s+75 μm (No.2), 240 W+450 mm/s+90 μm (No.3), 240 W+500 mm/s+90 μm (No.4)。测得上述四组参数下 $\text{TiB}_2/7050$ 复合材料试样的相对密度分别约为 98.3%、98.7%、98.5% 和 99.1%。之后对这四组试样进行金相组织观测,结果如图 3 所示。可以看到,这四组试样的金相组织并不存在

裂纹,孔隙缺陷由虚线圈出。研究结果表明造成 LPBF 成形 7050 铝合金力学性能不佳的主要原因是裂纹的产生^[24]。根据本实验结果,发现 TiB₂颗粒可以明显抑制 LPBF 过程中样品裂纹的产生,TiB₂/7050 复合材料的可打印性相比 7050 铝合金得到了明显的提高。

3.2 试样块的力学性能及分析

在上述四组参数下,利用 LPBF 成形尺寸为 60 mm×20 mm×12 mm 的样块,并对沉积态和热处理态试样进行室温拉伸实验,试样的抗拉强度、屈服

强度及延伸率如图 4 所示。在 240 W+450 mm/s+75 μm(No.1)打印参数下成形的 TiB₂/7050 复合材料沉积态试样的强度最高,抗拉强度、屈服强度及延伸率分别为 286 MPa、250 MPa 和 2.3%。经过热处理后,在四组参数条件下成形材料的强度及塑性有了明显提高,其中在 240 W+450 mm/s+75 μm(No.1)打印参数下成形的材料的抗拉强度、屈服强度及延伸率分别达到 351 MPa、294 MPa 和 4.2%。本文的结果接近目前现有文献^[19-20]报道的颗粒增强 7050 铝合金的力学性能。

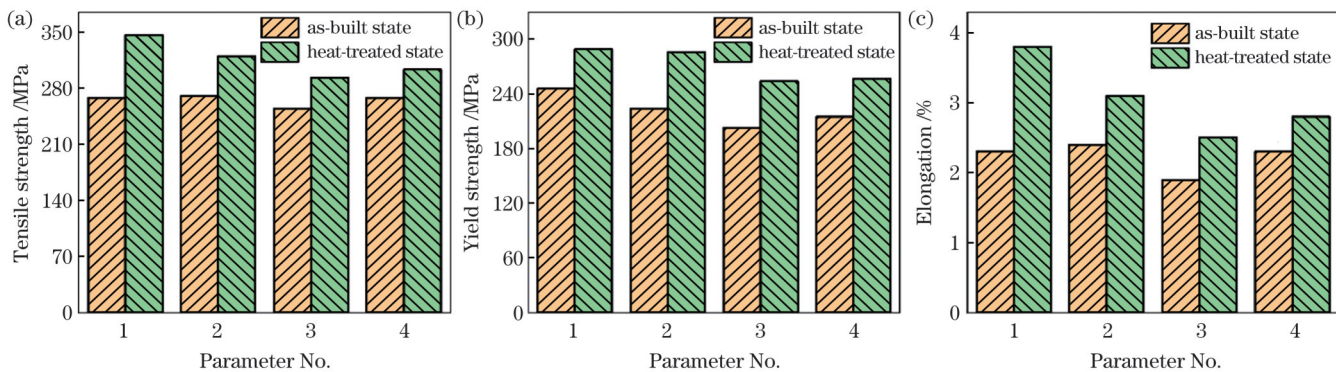


图 4 沉积态和热处理态 LPBF 成形 TiB₂/7050 复合材料的力学性能。(a)抗拉强度;(b)屈服强度;(c)延伸率

Fig. 4 Mechanical properties of as-built and heat-treated TiB₂/7050 composites formed by LPBF. (a) Tensile strength; (b) yield strength; (c) elongation

图 5 为在 240 W+450 mm/s+75 μm(No.1)工艺参数条件下 LPBF 成形 TiB₂/7050 复合材料的 X 射线衍射(XRD)结果。可以明显看到,沉积态和热处理态 TiB₂/7050 复合材料的 XRD 谱有明显的 α-Al 和 TiB₂ 衍射峰。热处理后,可以在 XRD 图谱中观察到 η' 相(MgZn₂)衍射峰的存在^[25]。此外,在两种状态下的 XRD 结果中没有观察到其他衍射峰。

图 6 为在 240 W+450 mm/s+75 μm(No.1)工艺参数条件下 LPBF 成形 TiB₂/7050 复合材料沉积态和

热处理态的 SEM 和 EDS 结果。在沉积态下,复合材料的主要组织为 α-Al 相及 TiB₂ 颗粒。复合材料经热处理后,由 SEM 结果可以看出,大量点状相及长条状的第二相从基体中析出,由文献[26]可知其为 η' 相。TiB₂ 颗粒可以使材料中 η' 相的析出激活能更低^[27],从而促进 η' 相的析出。η' 相不容易被剪切,在变形过程中一般不会被可动位错切过,当位错运动到 η' 相周围时一般会发生 Orowan 强化,从而出现 Orowan 绕过机制^[28]。此外,由 EDS 结果可以看到含 Cu 的 η' 相的析出,大量的强化相析出使得热处理后复合材料的强度明显增大。在时效过程中,Cu 元素溶入到过渡 η' 相中,提高了过渡 η' 相的稳定性,减缓了其转变为 η 相的速度,保证材料在时效阶段具有较高的力学性能。

TiB₂/7050 复合材料(TiB₂ 颗粒的质量分数为 7%)采用 LPBF 成形工艺,由于颗粒的存在以及较高的冷却速率,在 LPBF 过程中能够诱发大量位错的生成,在拉伸过程中发生位错的塞积,从而提高材料的强度。位错强化($\Delta\sigma_d$)^[29]可以表示为

$$\Delta\sigma_d = aMGb\sqrt{\rho_{total}}, \quad (1)$$

式中:a 为点阵常数(取 0.405);M 为泰勒因子(取 3.06);G 为铝的剪切模量(取 26.9);b 为 Burgers 矢量大小(取 0.286); ρ_{total} 为位错密度,可以通过透射电子显微镜(TEM)等表征手段获得。此外, $\Delta\sigma_{Orowan}$ 为 TiB₂

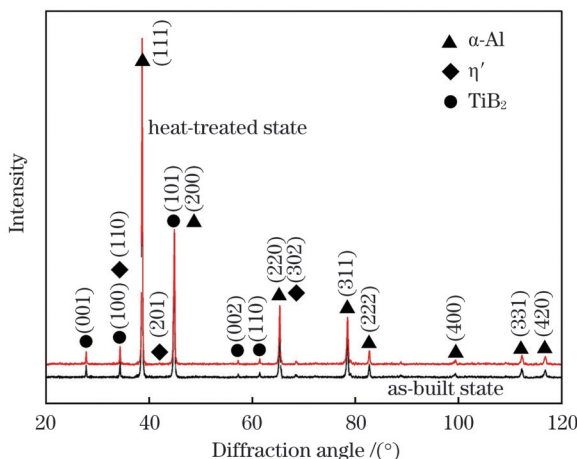


图 5 沉积态和热处理态 TiB₂/7050 复合材料的 XRD 谱
Fig. 5 XRD patterns of as-built and heat-treated TiB₂/7050 composites

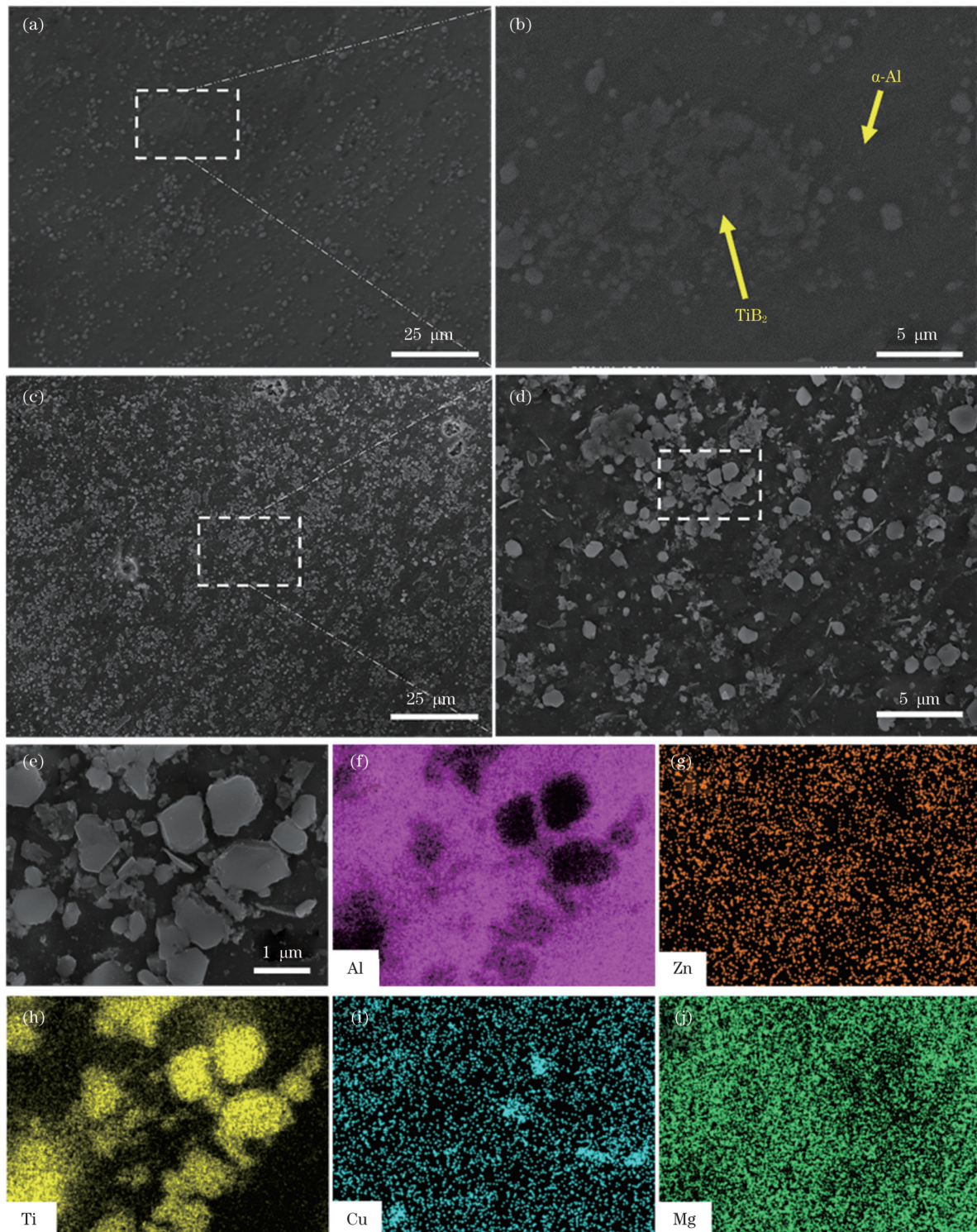


图 6 沉积态和热处理态 $\text{TiB}_2/7050$ 复合材料的 SEM 图像和 EDS 结果。(a)(b)沉积态和(c)~(e)热处理态 $\text{TiB}_2/7050$ 复合材料的 SEM 图像;沉积态及热处理态 $\text{TiB}_2/7050$ 复合材料中的(f)Al、(g)Zn、(h)Ti、(i)Cu、(j)Mg 的 EDS 结果

Fig. 6 SEM images and EDS results of as-built and heat-treated $\text{TiB}_2/7050$ composites. SEM images of (a)(b) as-built and (c)–(e) heat-treated $\text{TiB}_2/7050$ composites; EDS results of (f) Al, (g) Zn, (h) Ti, (i) Cu, and (j) Mg in as-built and heat-treated $\text{TiB}_2/7050$ composites

颗粒引入的 Orowan 强化^[30], 可以表示为

$$\Delta\sigma_{\text{Orowan}} = \frac{\phi G b}{d_p} \left(\frac{6V_p}{\pi} \right)^{\frac{1}{3}}, \quad (2)$$

式中: ϕ 为与材料相关的常数(取 2); V_p 为纳米颗粒的

体积分数(约为 3.9%); d_p 为纳米颗粒的平均尺寸(约为 100 nm)。计算得 $\Delta\sigma_{\text{Orowan}}$ 约为 69 MPa。

图 7 为在 240 W+450 mm/s+75 μm (No.1)工艺参数条件下 LPBF 成形 $\text{TiB}_2/7050$ 复合材料热处理态垂直于打印方向的晶粒分布图, 其中 X、Y、Z 分别

为晶体的三个晶向。由图 7 可知, LPBF 成形的 $\text{TiB}_2/7050$ 复合材料的晶粒组织呈等轴晶分布, 等轴晶界以大角度(角度 $>15^\circ$)晶界为主, 晶粒尺寸集中在 $1\sim3\ \mu\text{m}$ 区间。此外, $\text{TiB}_2/7050$ 复合材料热处理态的组织的最大强度值为随机密度(M)的 1.46 倍。在 LPBF 过程中, 金属粉末迅速熔化并冷却, 具有高

温度梯度和极快的冷却速率^[31]。在 LPBF 过程中, 晶粒一般会发生外延生长, 形成粗大的柱状晶, 添加异质形核剂后可实现晶粒细化, 并形成比铸造组织更加细小的等轴晶。此外, TiB_2 颗粒作为异质形核的质点, 可以促进 $\text{TiB}_2/7050$ 复合材料的非均匀形核^[32]。

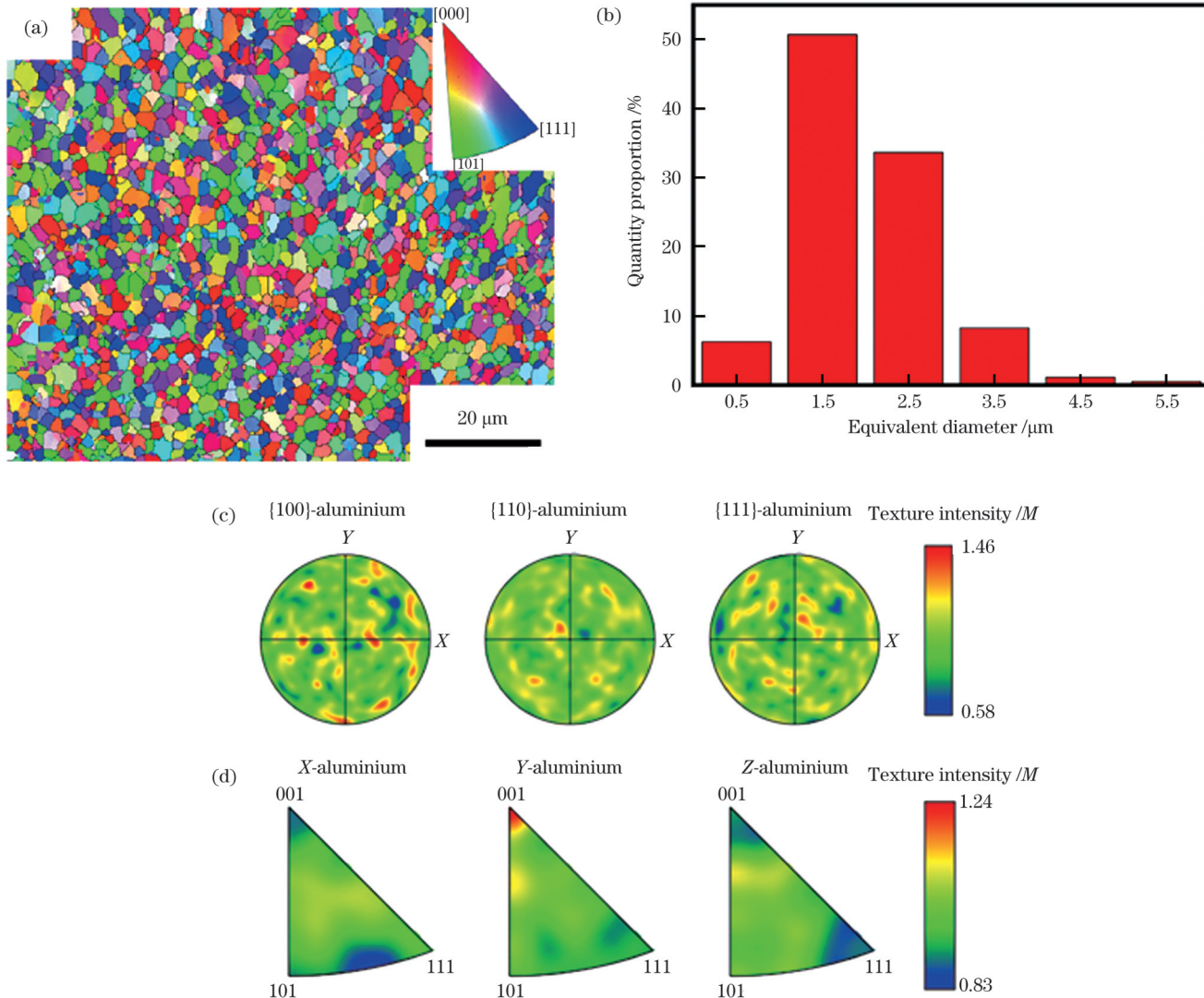


图 7 LPBF 成形 $\text{TiB}_2/7050$ 复合材料热处理态的 EBSD 图像、晶粒尺寸分布、极图和反极图。(a) EBSD 图像;(b) 晶粒尺寸分布图;(c) 极图;(d) 反极图

Fig. 7 EBSD image, grain size distribution, and pole and inverse pole images of heat-treated $\text{TiB}_2/7050$ composites formed by LPBF.
(a) EBSD image; (b) grain size distribution; (c) pole image; (d) inverse pole image

图 8 为在 240 W+450 mm/s+ $75\ \mu\text{m}$ (No.1)参数条件下 LPBF 成形 $\text{TiB}_2/7050$ 复合材料沉积态和热处理态的拉伸断口形貌。可以看到, 两种状态的宏观断口下断面处有大量的孔洞[图 8(a)和图 8(c)], 沉积态的断口处可见小尺寸解理平面和台阶[图 8(a)和图 8(b)], 且断口韧窝的数量较少, 呈现出明显的脆性断裂。在加载变形过程中, 材料整体的孔隙度和孔径会随着变形量的增大而增大^[33-34], 原有微米级孔洞长大, 微孔合并^[35], 产生新的孔洞缺陷^[36-37], 最终材料出现颈缩破坏。此外, 在 $\text{TiB}_2/7050$ 复合材料

的断口处有少量的短裂纹, 在拉伸过程中短裂纹会严重影响材料的塑性和强度。从图 8(c)和图 8(d)可以看出, 热处理后, $\text{TiB}_2/7050$ 复合材料的断口呈现出典型的韧窝特征, 同时也有一些区域表现出脆性断裂的解理平台特征, 这属于混合型的韧性-脆性断裂, 其中韧窝尺寸为 $2\sim3\ \mu\text{m}$, 与晶粒尺寸相当。 TiB_2 颗粒主要分布在韧窝底部, 这表明 TiB_2 颗粒可以限制晶界在拉伸过程中的移动, 且热处理后韧窝较深, 韧窝底部有更多的第二相颗粒, 材料力学性能进一步提升。

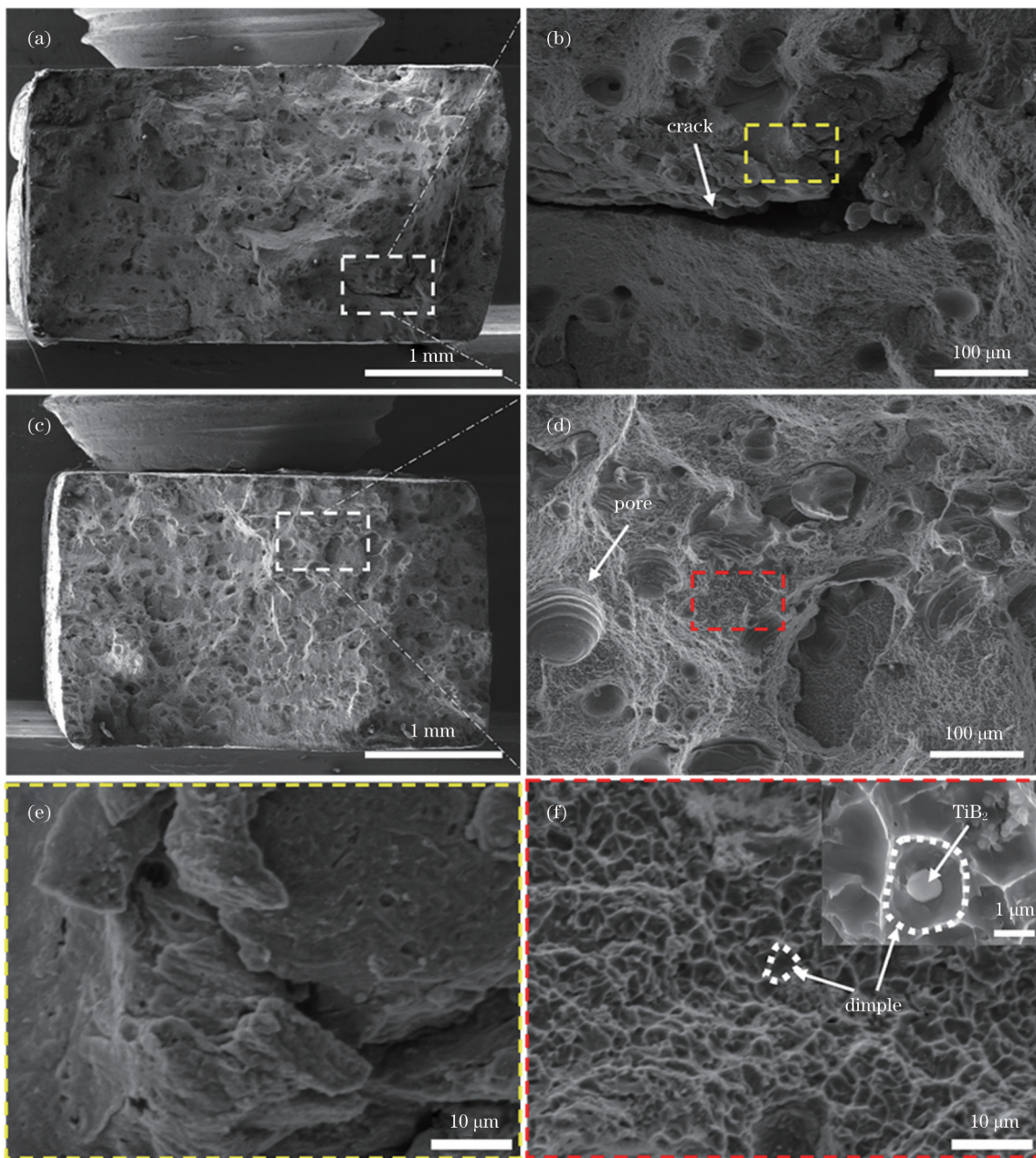


图 8 沉积态和热处理态 $\text{TiB}_2/7050$ 复合材料的拉伸断口形貌。(a)(b)沉积态;(c)(d)热处理态;(e)图 8(b)虚线框处的放大结果;(f)图 8(d)虚线框处的放大结果

Fig. 8 Tensile fracture morphologies of as-built and heat-treated $\text{TiB}_2/7050$ composites. (a)(b) As-built state; (c)(d) heat-treated state; (e) enlarged result at dotted box in Fig. 8 (b); (f) enlarged result at dotted box in Fig. 8 (d)

4 结 论

通过在 7050 合金中引入原位自生纳米 TiB_2 颗粒, 显著抑制了 LPBF 成形 7050 铝合金的裂纹产生, 材料表现出较好的成形性。在 240 W + 450 mm/s + 75 μm (No. 1) 打印参数下 $\text{TiB}_2/7050$ 复合材料的强度最高, 其抗拉强度、屈服强度及延伸率分别为 286 MPa、250 MPa 和 2.3%。进一步对 $\text{TiB}_2/\text{Al-Cu-Mg}$ 复合材料 (TiB_2 的质量分数为 4%) 进行后热处理研究, 通过调控析出相的尺寸和数量, 获得了具有较高强度和伸长率的增材制造复合材料。LPBF 成形的 $\text{TiB}_2/7050$ 复

合材料经热处理后, 其抗拉强度、屈服强度和伸长率分别为 351 MPa、294 MPa 和 4.2%。研究结果为增材制造纳米颗粒增强铝基复合材料及其后处理提供了理论参考。

参 考 文 献

- [1] Wang A, Wang H Z, Wu Y, et al. 3D printing of aluminum alloys using laser powder deposition: a review[J]. The International Journal of Advanced Manufacturing Technology, 2021, 116(1/2): 1-37.
- [2] Wei M W, Chen S Y, Xi L Y, et al. Selective laser melting of 24CrNiMo steel for brake disc: fabrication efficiency, microstructure evolution, and properties[J]. Optics & Laser Technology, 2018, 107: 99-109.

- [3] Mu J R, Sun T T, Leung C L A, et al. Application of electrochemical polishing in surface treatment of additively manufactured structures: a review[J]. *Progress in Materials Science*, 2023, 136: 101109.
- [4] 孙腾腾, 王洪泽, 吴一, 等. 原位自生 2% TiB₂ 颗粒对 2024Al 增材制造合金组织和力学性能的影响[J]. *金属学报*, 2023, 59(1): 169-179.
- Sun T T, Wang H Z, Wu Y, et al. Effect of *in situ* 2% TiB₂ particles on microstructure and mechanical properties of 2024Al additive manufacturing alloy[J]. *Acta Metallurgica Sinica*, 2023, 59(1): 169-179.
- [5] Gao Z Y, Wang H Z, Letov N, et al. Data-driven design of biometric composite metamaterials with extremely recoverable and ultrahigh specific energy absorption[J]. *Composites Part B: Engineering*, 2023, 251: 110468.
- [6] 郭朦, 戴延丰, 黄斌达. 典型航空机电产品激光粉末床熔融技术应用现状与发展[J]. *中国激光*, 2023, 50(16): 1602304.
- Guo M, Dai Y F, Huang B D. Application status and development of laser powder bed fusion technology in typical electromechanical aviation products[J]. *Chinese Journal of Lasers*, 2023, 50(16): 1602304.
- [7] Karolus M, Maszybrocka J, Stwora A, et al. Residual stresses of AlSi10Mg fabricated by selective laser melting (SLM)[J]. *Archives of Metallurgy and Materials*, 2029, 64: 1011-1016.
- [8] 赵钰涣, 龙芋宏, 徐榕蔚, 等. 7075 铝合金选区激光熔化研究现状[J]. *现代制造工程*, 2021(9): 146-151.
- Zhao Y H, Long Y H, Xu R W, et al. Research status of selective laser melting in 7075 aluminum alloy[J]. *Modern Manufacturing Engineering*, 2021(9): 146-151.
- [9] DebRoy T, Wei H L, Zuback J S, et al. Additive manufacturing of metallic components-process, structure and properties[J]. *Progress in Materials Science*, 2018, 92: 112-224.
- [10] Liu P, Hu J Y, Li H X, et al. Effect of heat treatment on microstructure, hardness and corrosion resistance of 7075 Al alloys fabricated by SLM[J]. *Journal of Manufacturing Processes*, 2020, 60: 578-585.
- [11] Otani Y, Sasaki S. Effects of the addition of silicon to 7075 aluminum alloy on microstructure, mechanical properties, and selective laser melting processability[J]. *Materials Science and Engineering: A*, 2020, 777: 139079.
- [12] Zhou S Y, Su Y, Wang H, et al. Selective laser melting additive manufacturing of 7xxx series Al-Zn-Mg-Cu alloy: cracking elimination by co-incorporation of Si and TiB₂[J]. *Additive Manufacturing*, 2020, 36: 101458.
- [13] 沈君剑, 刘允中, 欧阳盛, 等. 激光选区熔化成形 TiB₂ 与 SiC 颗粒混杂增强铝基复合材料的显微组织与力学性能[J]. *粉末冶金材料科学与工程*, 2020, 25(3): 251-259.
- Shen J J, Liu Y Z, Ouyang S, et al. Microstructures and mechanical properties of aluminum matrix composites reinforced with hybrid TiB₂ and SiC prepared by selective laser melting[J]. *Materials Science and Engineering of Powder Metallurgy*, 2020, 25(3): 251-259.
- [14] Tan Q Y, Fan Z Q, Tang X Q, et al. A novel strategy to additively manufacture 7075 aluminium alloy with selective laser melting[J]. *Materials Science and Engineering: A*, 2021, 821: 141638.
- [15] Yi J L, Chang C, Yan X C, et al. A novel hierarchical manufacturing method of the selective laser melted Al 7075 alloy [J]. *Materials Characterization*, 2022, 191: 112124.
- [16] Hu J Y, Liu P, Sun S Y, et al. Relation between heat treatment processes and microstructural characteristics of 7075 Al alloy fabricated by SLM[J]. *Vacuum*, 2020, 177: 109404.
- [17] Martin J H, Yahata B D, Hundley J M, et al. 3D printing of high-strength aluminium alloys[J]. *Nature*, 2017, 549(7672): 365-369.
- 吕新蕊, 刘婷婷, 廖文和, 等. 高强铝合金 7075 激光粉末床熔融凝固裂纹的消除与质量控制[J]. *中国激光*, 2022, 49(14): 1402209.
- Lü X R, Liu T T, Liao W H, et al. Solidification crack elimination and quality control of high-strength aluminum alloy
- 7075 fabricated using laser powder bed fusion[J]. *Chinese Journal of Lasers*, 2022, 49(14): 1402209.
- [19] Mertens R, Baert L, Vanmeensel K, et al. Laser Powder bed fusion of high strength aluminum[J]. *Material Design & Processing Communications*, 2021, 3(5): 161.
- [20] Li X W, Li G, Zhang M X, et al. Novel approach to additively manufacture high-strength Al alloys by laser powder bed fusion through addition of hybrid grain refiners[J]. *Additive Manufacturing*, 2021, 48: 102400.
- [21] 詹强坤, 刘允中, 刘小辉, 等. 激光选区熔化成形含锆 7xxx 系铝合金的显微组织与力学性能[J]. *材料工程*, 2021, 49(6): 85-93.
- Zhan Q K, Liu Y Z, Liu X H, et al. Microstructures and mechanical properties of zirconium-containing 7xxx aluminum alloy prepared by selective laser melting[J]. *Journal of Materials Engineering*, 2021, 49(6): 85-93.
- [22] Zhou L, Pan H, Hyer H, et al. Microstructure and tensile property of a novel AlZnMgScZr alloy additively manufactured by gas atomization and laser powder bed fusion[J]. *Scripta Materialia*, 2019, 158: 24-28.
- [23] Sun T T, Chen J, Wu Y, et al. Achieving excellent strength of the LPBF additively manufactured Al-Cu-Mg composite *via in situ* mixing TiB₂ and solution treatment[J]. *Materials Science and Engineering: A*, 2022, 850: 143531.
- [24] Zheng T Q, Pan S H, Murali N, et al. Selective laser melting of novel 7075 aluminum powders with internally dispersed TiC nanoparticles[J]. *Materials Letters*, 2022, 319: 132268.
- [25] Liu Y X, Wang R C, Peng C Q, et al. Microstructural evolution and mechanical performance of *in situ* TiB₂/AlSi10Mg composite manufactured by selective laser melting[J]. *Journal of Alloys and Compounds*, 2021, 853: 157287.
- [26] Mason C J T, Rodriguez R I, Avery D Z, et al. Process-structure-property relations for as-deposited solid-state additively manufactured high-strength aluminum alloy[J]. *Additive Manufacturing*, 2021, 40: 101879.
- [27] 欧阳盛, 刘允中, 沈君剑, 等. (TiH₂+TiB₂)/AA7075 复合粉末激光选区熔化成形的显微组织与力学性能[J]. *粉末冶金材料科学与工程*, 2020, 25(3): 197-205.
- Ouyang S, Liu Y Z, Shen J J, et al. Microstructure and mechanical properties of selective laser melting of (TiH₂+TiB₂)/AA7075 composite powders[J]. *Materials Science and Engineering of Powder Metallurgy*, 2020, 25(3): 197-205.
- [28] Yan S J, Wang R C, Peng C Q, et al. Enhancing mechanical properties of 7055 Al alloy by adding 1 wt.% Mg and tailoring the precipitations[J]. *Journal of Alloys and Compounds*, 2023, 947: 169536.
- [29] Ma K K, Wen H M, Hu T, et al. Mechanical behavior and strengthening mechanisms in ultrafine grain precipitation-strengthened aluminum alloy[J]. *Acta Materialia*, 2014, 62: 141-155.
- [30] Zhang J L, Song B, Yang L, et al. Microstructure evolution and mechanical properties of TiB/Ti6Al4V gradient-material lattice structure fabricated by laser powder bed fusion[J]. *Composites Part B: Engineering*, 2020, 202: 108417.
- [31] Hooper P A. Melt pool temperature and cooling rates in laser powder bed fusion[J]. *Additive Manufacturing*, 2018, 22: 548-559.
- [32] Liu G, Geng J W, Li Y G, et al. Microstructures evolution of nano TiB₂/7050 Al composite during homogenization[J]. *Materials Characterization*, 2020, 159: 110019.
- [33] Chai H W, Fan D, Yuan J C, et al. Deformation dynamics of a neutron-irradiated aluminum alloy: an *in situ* synchrotron tomography study[J]. *Acta Materialia*, 2023, 243: 118493.
- [34] 石岩, 魏登松. 激光粉末床熔融增材制造未熔合气孔缺陷形成机理研究[J]. *中国激光*, 2023, 50(20): 2002303.
- Shi Y, Wei D S. Lack-of-fusion porosity defects formation mechanism in laser powder bed fusion additive manufacturing[J]. *Chinese Journal of Lasers*, 2023, 50(20): 2002303.
- [35] Wang Y F, Toda H, Xu Y T, et al. *In-situ* 3D observation of hydrogen-assisted particle damage behavior in 7075 Al alloy by

- [35] synchrotron X-ray tomography[J]. Acta Materialia, 2022, 227: 117658.
- [36] Croom B P, Jin H, Noell P J, et al. Collaborative ductile rupture mechanisms of high-purity copper identified by *in situ* X-ray computed tomography[J]. Acta Materialia, 2019, 181: 377-384.
- [37] 宋长辉, 付厚雄, 严仲伟, 等. 激光粉末床熔融成形内部质量缺陷及其调控方法[J]. 中国激光, 2022, 49(14): 1402801.
Song C H, Fu H X, Yan Z W, et al. Internal defects and control methods of laser powder bed fusion forming[J]. Chinese Journal of Lasers, 2022, 49(14): 1402801.

Microstructure and Properties of 7050 Aluminum Matrix Composites Reinforced by TiB₂ Particles Fabricated Through Laser Powder Bed Fusion (Invited)

Wang An¹, Tang Zijue^{1,2}, Wu Yi^{1,2}, Wang Haowei^{1,2}, Wang Hongze^{1,2*}

¹The State Key Laboratory of Metal Matrix Composites, School of Materials Science and Engineering, Shanghai Jiao Tong University, Shanghai 200240, China;

²Institute of Anhui (Huabei) Alumics Materials, Shanghai Jiao Tong University, Huabei 235000, Anhui, China

Abstract

Objective Laser powder bed fusion (LPBF) is a metal additive manufacturing technology that utilizes high-power lasers to melt and stack powdered materials for rapid prototyping. However, metals used in current lightweight and high-strength LPBF processes are extremely limited. In particular, in terms of aluminum alloys, LPBF-formed aluminum alloys are mainly focused on Al-Si alloys. The inherent un-weldability of 7050 aluminum alloy and the high thermal stress induced by rapid cooling during the additive manufacturing process cause cracking or deformation during LPBF, limiting the application of LPBF technology in the preparation of this type of alloys. This study investigates the LPBF formation of TiB₂/7050 composite and subsequent heat treatment (solution + aging treatment) process, exploring the effects of different process parameters and heat treatment conditions on the microstructures and room temperature tensile properties of TiB₂/7050 composite.

Methods Orthogonal methods are employed to select laser process parameters, including laser power levels of 210, 225, 240, and 255 W. The scanning speed levels are set at 400, 450, 500, 550, and 600 mm/s, whereas hatch spacings are set at 75 μm and 90 μm. The scanning strategy involves a layer-by-layer rotation of 90° using the stripe scanning method. In total, there are 40 sets of process parameters. The heat treatment is conducted via solution treatment in an muffle furnace. After the samples are solubilized at 475 °C for 1 h, they are cooled in room temperature water and then aged at 120 °C for 12 h in a tubular resistance furnace before final cooling in ambient air. Tensile experiments are performed using a room temperature tensile device at a strain rate of 10⁻⁴ s⁻¹. Tensile specimens with appropriate dimensions are prepared, and three samples in equivalent conditions are tested to obtain the average values. X-ray diffractometer is employed to analyze the phase composition of the samples. The scan angle range is set between 20° and 120° with a scan rate of 2 (°)/min. Microstructural characterization is performed using a scanning electron microscope (SEM), and the material surface elemental compositions are analyzed using an energy-dispersive spectrometer (EDS).

Results and Discussions Under the following four sets of process parameters (laser power + scanning speed + scanning spacing), the relative densities of the printed sample are higher: 240 W+450 mm/s+75 μm (No.1), 240 W+500 mm/s+75 μm (No.2), 240 W+450 mm/s+90 μm (No.3), and 240 W+500 mm/s+90 μm (No.4). The obtained relative densities of TiB₂/7050 composite samples are approximately 98.3%, 98.7%, 98.5%, and 99.1%, respectively (Fig. 2). The tensile experiments under these four sets of parameters are conducted at room temperature on the as-built and heat-treated samples. In the as-built state, the TiB₂/7050 composite exhibits the highest strength under the condition 240 W+450 mm/s+75 μm (No.1), with tensile strength, yield strength, and elongation being 286 MPa, 250 MPa, and 2.3%, respectively (Fig. 4). After heat treatment, both the strength and plasticity of the material significantly improve for all four sets of parameters. In particular, under the as-built condition of 240 W+450 mm/s+75 μm (No.1), the material achieves tensile strength, yield strength, and elongation values of 351 MPa, 294 MPa, and 4.2%, respectively (Fig. 4). Additionally, in the as-built state, the primary microstructure of the composite consists of α-Al phases and TiB₂ particles. After heat treatment, a significant number of secondary phases precipitate from the matrix, and SEM results show the presence of abundant precipitates in the forms of both particles and elongated phases (Fig. 6).

Conclusions The addition of TiB₂ particles significantly suppresses the cracking of 7050 alloys through the LPBF process and exhibits favorable formability. The optimal process parameters in the as-built state are 240 W+450 mm/s+75 μm, which result in the highest strength of the TiB₂/7050 composite. The tensile strength, yield strength, and elongation are 286 MPa, 250 MPa, and 2.3%, respectively. The microstructure of the TiB₂/7050 composite after heat treatment consists of fine-sized equiaxed grains. The grain size is concentrated in the range of 1–3 μm, with TiB₂ particles evenly dispersed in the grain boundaries and within the equiaxed grain structure, effectively promoting the formation of heterogeneously nucleated refined grains. After heat treatment, the tensile strength, yield strength, and elongation of the specimens of TiB₂/7050 composite are 351 MPa, 294 MPa, and 4.2%, respectively.

Key words laser technique; laser powder bed fusion; TiB₂/7050 composite; heat treatment; mechanical properties